RARE METALS

ORIGINAL ARTICLE

Microstructure and properties of Inconel 625 + WC composite coatings prepared by laser cladding

Zhi-Hua Tian [iD] , **Yong-Tao Zhao*** [iD] , **Ya-Jun Jiang, Hui-Ping Ren**

Abstract Inconel 625 + WC composite coatings were prepared on the surface of 2Cr13 steel by laser cladding. The microstructure, microhardness and corrosion resistance of the composite coatings with different WC contents were investigated in detail. The results show that the phase compositions of the composite coatings are mainly γ-(Ni, Fe) and various carbides. The content of WC has a significant effect on the microstructure of the cladding layers. When the WC content is 10 wt% and 15 wt%, the cladding layer has developed columnar dendrites. However, the 20 wt% WC coating is mainly composed of cellular dendrites and columnar dendrites. With the increase in WC content, the average hardness of the composite coating gradually increases. The average hardness of 20 wt% WC coating is the highest (HV$_1$ 536.98), which is a factor of 2.64 greater than that of the 2Cr13 steel matrix. Electrochemical results show that all the composite coatings have better corrosion resistance than 2Cr13 steel in 0.5 mol·L^{-1} HCl solution. The composite coating with 10 wt% WC has the best corrosion resistance, its corrosion potential (E_{corr}) is 0.78806 V higher than that of 2Cr13 steel, and the corrosion current density (I_{corr}) is only 0.86% that of 2Cr13 steel.

Keywords Laser cladding; WC content; Inconel 625; Electrochemical corrosion; Microhardness

Z.-H. Tian, Y.-T. Zhao*, Y.-J. Jiang, H.-P. Ren
School of Material and Metallurgy, Inner Mongolia University
of Science and Technology, Baotou 014010, China
e-mail: zyt0011@126.com

1 Introduction

Turbine blades are the main components of the blast furnace gas residual pressure recovery turbine (top pressure recovery turbines, TRT). 2Cr13 stainless steel has been widely used as the main material of TRT blades because of its high fatigue strength and good comprehensive mechanical properties [1]. Because of their long-term operation in high-speed, dust-containing and corrosive media environments, TRT blades will suffer severe erosion, wear and corrosion, which greatly reduces the functional accuracy of the original design, causing the blades to fail prematurely [2, 3]. Owing to their high-precision requirements, repairing the blades by traditional methods such as built-up welding will cause blade deformation, making it difficult to ensure their original sizes while also being a time-consuming process [4]. To make TRT blades safe and reliable for longer service time, adding a protective coating on the surface can be a cost-effective method. However, due to their poor adhesion with the matrix, coatings prepared by electroplating or spraying technology may fall off during operation [5, 6]. As a new surface modification technology, coatings obtained by laser cladding have fine and compact structures and can metallurgically bond with the matrix, which can greatly improve the wear resistance and corrosion resistance of the TRT blades, thereby improving the service life of materials [7–9]. The most typical powder for coating preparation by laser cladding technology is Ni-based alloy powder which has good self-deoxidization, good wettability and high-temperature strength [10, 11]. Inconel 625 superalloy cladding powder consists of an austenitic matrix phase with fcc structure and secondary phases such as carbides, intermetallic compounds (e.g., Ni$_3$Nb) and Laves [12–14].

It has excellent high-temperature chlorine corrosion resistance [15–17], but its hardness is low ($\sim$ HV$_1$ 213), which is not conducive for using as a single coating material in an environment where wear occurs. To further improve the wear resistance of the cladding layer, a certain amount of hard ceramic powder (such as WC, TiC and SiC) is often added to the Ni matrix powder [18]. Among the additives, WC powder is a hard material with excellent wear resistance and is widely used in surface engineering [19]. However, as a result of the large difference between the melting points, linear expansion coefficients, elastic modulus and thermal conductivities of the ceramic material and the metal matrix, large thermal stress is easily generated during the cladding process, causing defects such as cracks and holes in the cladding layer [20]. Hence, it is particularly important to obtain a reasonable amount of WC powder. Some of the studies have addressed the evolution of WC-particle-reinforced Ni-based alloy coating properties with changes in WC content [19, 21].

To avoid the defects caused by the difference between two thermal expansion coefficients, several studies have been done to investigate the influences of the high-power conditions on laser cladding WC-particle-reinforced Ni-based alloy coatings. In this case, WC particles were melted or reacted in the Ni matrix and inter-diffused with the matrix elements to form and precipitate secondary carbide phases during solidification, resulting in the significant changes in the properties of the composite coating [22, 23]. To further investigate the effects of the dissolution of WC particles and the precipitation of secondary carbides on the microstructure and properties of the coatings, in this study, Inconel 625 + WC composite coatings were prepared on the 2Cr13 steel substrate by laser cladding technology. The effects of WC particle content on the microstructure, phase composition, microhardness and corrosion resistance of the composite coatings were studied in detail. The results can provide a useful reference for surface strengthening of TRT blades.

2 Experimental

2.1 Materials

2Cr13 martensitic stainless steel was used as the substrate material, and the sample size was 100 mm × 100 mm × 10 mm. The substrate was firstly mechanically ground to remove the surface oxide scale, then sanded with sandpaper and cleaned with absolute ethanol to dislodge surface oil. The cladding materials were WC + Inconel 625 mixed powders in which the WC content was 10 wt%, 15 wt%

and 20 wt%, respectively. The size of Inconel 625 powder particles used in the experiment ranged from 53 to 125 μm in diameter, and the chemical compositions are given in Table 1. The WC used in the experiment was a high-purity cobalt-coated tungsten carbide powder in which the content of Co was 8.13 wt% and the particle diameter was 15–45 μm. Different proportions of WC and Inconel 625 powder were mixed in a planetary ball mill (TJ-2L, China) at 300 r·min^{-1} for 2 h. The mixed powder was then placed in a constant-temperature oven (200 °C) for 2 h before conducting the laser cladding experiments.

2.2 Methods

Laser cladding was conducted using an IPG (Germany) fiber laser with a wavelength of 1070 nm and the spot size of 12 mm × 1 mm, while the position of the laser was adjusted by a KUKA (Germany) six-axis linkage robot. The mixed powders were synchronously fed into the molten pool by the powder feeder, and the optimized process parameters obtained in the previous stage were as follows: laser power of 2400 W, powder feeding rate of 15 g·min^{-1} and scanning speed of 5 mm·s^{-1}. Argon gas with flow rates of 10 and 5 L·min^{-1} was used as shielding and powder-carrying gas, respectively. The cladding experiment entailed a single-pass and multi-layer superposition method to obtain a certain thickness. After each layer was melted, the oxide scale on the surface of the cladding layer was cleaned using a wire brush, and a total of four layers were coated. The schematic diagram of the laser cladding process is shown in Fig. 1.

A molybdenum wire-cutting machine was used to cut the cladding layered sample to a size of 10 mm × 10 mm × 10 mm. Cross sections perpendicular to the cladding direction were selected for inlaying. After grinding and polishing, an aqua regia solution (HNO$_3$/HCl = 1:3, vol%) was used to corrode the samples for 15–20 s. The qualities and morphologies of the cladding layers were analyzed by using a Jiangnan MR3000 optical microscope (OM) and a QUANTA FEG 450 field emission scanning electron microscope (FESEM) equipped with an energy-dispersive spectrometer (EDS). The phase compositions of the cladding layers were analyzed by a D8 ADVANCE X-ray diffractometer (XRD). Electron probe microanalysis (EPMA) X-ray elemental maps were obtained using a 5

Table 1 Chemical compositions of Inconel 625 alloy powder (wt%)

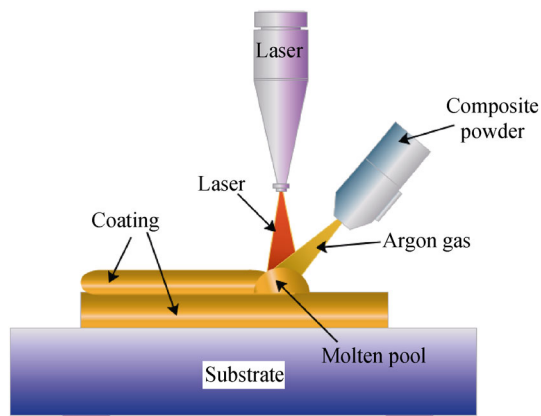| C	Cr	Si	Fe	Mo	Nb	Ni
0.09	20.21	1.52	2.64	9.22	3.27	Bal.

Fig. 1 Schematic diagram of laser cladding process

WDS detector-equipped JXA-8530F PLUS electron microprobe. The microhardness of the cladding layers from the surface to the substrate was measured by an HVS-1000Z microhardness tester under a load of 9.8 N and a loading time of 10 s. To study the effects of WC addition on the corrosion resistance of composite coatings, the room-temperature electrochemical properties of three kinds of coatings and matrix samples in 0.5 mol·L^{-1} HCl solution prepared with deionized water were tested by using a Princeton VersaSTAT 3F electrochemical workstation. A three-electrode system was employed in the present study, in which a platinum foil, a saturated calomel electrode (SCE) and the specimen were used as auxiliary electrode, reference electrode and working electrode, respectively. The effective working area of the specimens was 1 cm^2. All the samples were immersed in the electrolyte solution for 1 h to stabilize the open-circuit potential. The scanning range of the potentiodynamic polarization curve was -1.2 to 1.2 V, and the scanning rate was 0.5 mV·s^{-1}. An alternating current (AC) electrochemical impedance spectroscopy (EIS) test was performed at the open-circuit potential with a voltage amplitude of 10 mV and a frequency range of 1×10^{-2} to 1×10^4 Hz.

3 Results and discussion

3.1 Microstructural characteristics

Figure 2 shows cross-sectional macroscopic morphologies of the laser cladding WC + Inconel 625 composite coatings. It can be seen that all the three coatings prepared by the optimized process parameters have no obvious defects such as cracks, pores or inclusions, the interfaces between the coatings and the substrates are flat, and the thicknesses of the coatings are approximately the same (1.0–1.2 mm). When WC content is 10 wt% or 15 wt%, the coating is

mainly composed of developed columnar dendrites. However, the coating structure exhibits obvious delamination when the WC content is 20 wt%. Because each layer has different corrosion resistance to aqua regia, the coating can be divided into three layers with different brightness.

The detailed microstructures of the composite coatings with different WC contents are shown in Fig. 3. It can be seen from Fig. 3a, d, g that all the three coatings have a white bright planar crystal ribbon at the bonding zone. This ribbon is the transition region between the substrate and the cladding layer, indicating that the coating forms good metallurgical bonds with the substrate [24]. The planar crystal thicknesses of the coatings with WC contents of 10 wt%, 15 wt% and 20 wt% are 14 μm (Fig. 3a), 6 μm (Fig. 3d) and 8 μm (Fig. 3g), respectively. For the composite coatings with WC contents of 10 wt% and 15 wt%, the microstructures are basically the same, and the structural features from the bonding zones to the top coatings are mainly planar crystal, cellular and columnar crystals, columnar dendrites and equiaxed crystals. As the solidification progresses, the number of cellular crystals in the coating gradually decreases, the number of columnar crystals increases and becomes thinner, and fine uniform equiaxed crystals appear in the region near the surface layer of the coating. The columnar crystals of the coating with 10 wt% WC content become slenderer and the secondary dendritic axis fines obviously at ~ 460 μm away from the substrate (Fig. 2a, b). When WC content is 15 wt%, the microstructure of the coating is refined obviously at ~ 280 μm away from the substrate. Compared with that of the 10 wt% WC coating, the microstructure of the 15 wt% WC coating is finer and has more compact and stronger directivity columnar dendrites, with the primary axis almost growing upward perpendicular to the fusion line. However, the microstructure of the coating with a WC content of 20 wt% changes significantly. The crystal morphologies from the bonding zone to the top coating are planar crystal, cellular crystals and columnar crystals, and cellular dendrites and columnar dendrites; no equiaxed crystals have appeared at the top of the coating. Moreover, when WC content is 20 wt%, there is no transition interface like that in the former two coatings. The structure changes from columnar and cellular crystals to cellular dendrites at ~ 280 μm away from the substrate and from cellular dendrites to columnar dendrites at ~ 720 μm away from the substrate.

According to the theory of rapid solidification [25, 26], the growth morphologies of the different regions of the cladding layer are mainly determined by the temperature gradient (G) and the solidification rate (R). When the laser sweeps through the cladding layer, the liquid metal in contact with the substrate forms a chilling solid–liquid interface with a high G and a low R at the front edge.
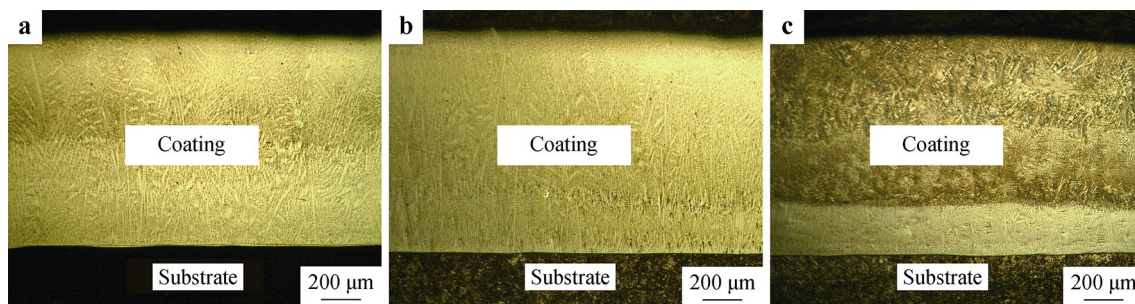
Fig. 2 Cross-sectional macroscopic images of composite coatings with WC contents of **a** 10 wt%, **b** 15 wt% and **c** 20 wt%
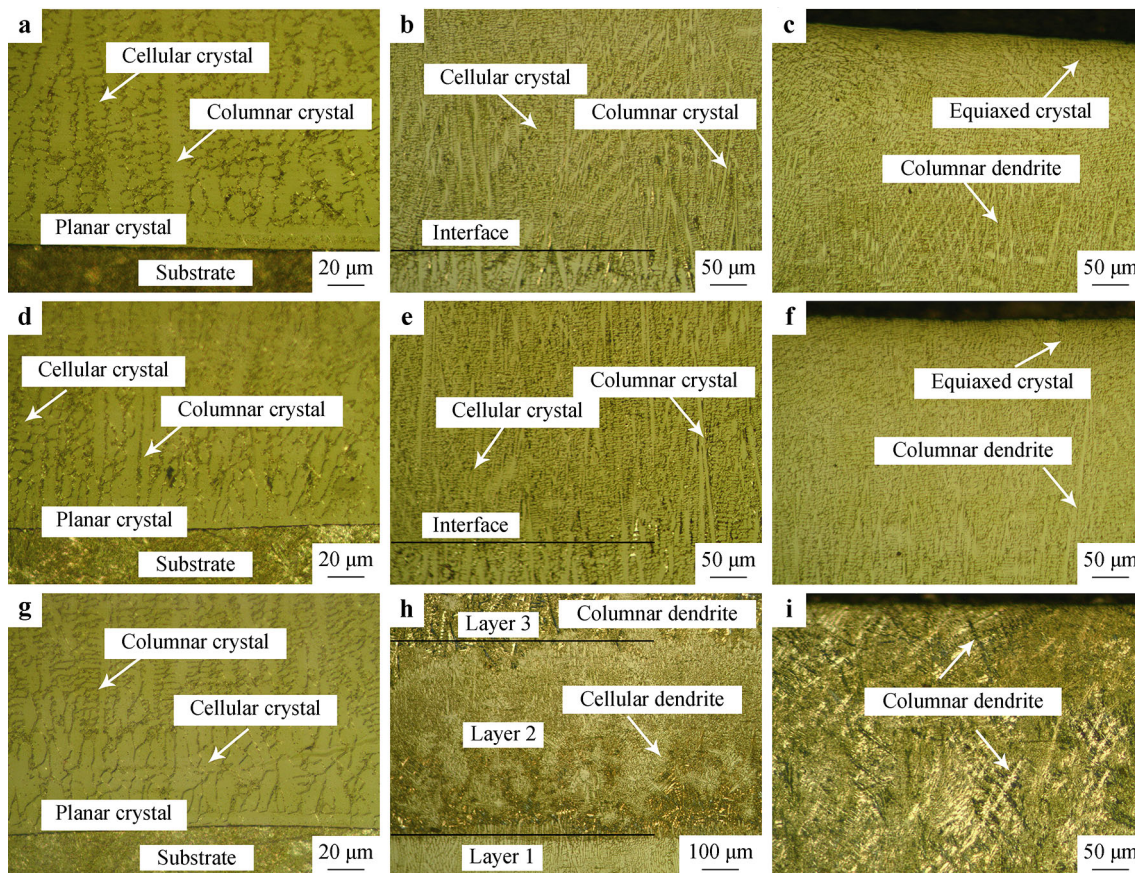
Fig. 3 OM images of composite coatings with WC contents of **a–c** 10 wt%, **d–f** 15 wt% and **g–i** 20 wt%

Therefore, the solidified structure at the bottom of the molten pool will grow upward in a planar crystal. As the distance from the fusion line increases, G gradually decreases while the undercooling at the planar crystal solid–liquid interface increases. At this time, numerous fine crystal nuclei are generated, thereby producing cellular crystals and columnar crystals. The redistribution of the solute atoms in the liquid phase at the front of the solid–liquid interface causes constitutional undercooling, and protrusions will be formed on the sides of the cellular crystals or columnar crystals. During the cladding process, heat dissipation in the middle of the molten pool is mainly carried out by the matrix, so the solidified structure tends to grow along the direction of maximum heat dissipation (i.e., perpendicular to the planar crystal). When the solidification reaches the surface of the molten pool, the upper part of the cladding layer can radiate heat in multiple directions to the surrounding environment (such as air). The melt is in a deep undercooled state, and the nucleation rate of the crystal is much higher than the growth rate. As a result, non-directional equiaxed crystals (Fig. 3c, f) and columnar dendrites (Fig. 3i) appear on the top of the coatings.

It should be noted that WC particles are not observed in these three composite coatings. The absorption coefficient

of WC for a fiber laser is much higher than that for the metal powder. During the experiment, some WC particles are burning and the remaining particles melt and react with the elements in the Ni alloy under the action of the high-energy laser beam to precipitate new carbides or intermetallic compounds. The formation of such precipitates can prevent the growth of γ-Ni dendrites in the bonding metal [21, 27]. For the upper and middle parts of the cladding layer, the 15 wt% WC coating produces more secondary carbides than the 10 wt% WC coating does, and therefore, it has a stronger inhibition effect on γ-Ni dendrites, resulting in the finer microstructure. For the bottom parts of the cladding layer, the actual content of WC in the molten pool decreases because of the dilution of the substrate, and the effect of WC is not obvious. Therefore, the underlying structure of the cladding layer is relatively coarse, and the structure transition interface appears like that in Fig. 3b, e. In contrast, when WC content increases to 20 wt%, increased absorption of the laser by WC minimizes the specific energy required to clad the coating with the same thickness. Therefore, although the process conditions for cladding the three coatings are the same, the temperature of entire molten pool for 20 wt% WC coating is higher and the temperature gradient in the liquid phase is smaller. This promoted the growth trend of γ-Ni dendrites and thus coarsened the microstructure of 20 wt% WC coating.

3.2 Phase analysis

Figure 4 shows surface XRD patterns of WC + Inconel 625 composite coatings. When WC content is 10 wt%, the composite coating is mainly composed of γ-(Ni, Fe), $M_{23}C_6$ and NbC. When WC content is 15 wt%, the phase of the coating is basically the same as that of 10 wt% WC,

Fig. 4 XRD patterns of laser cladding coatings with different contents of WC

but the diffraction intensity of the (200) crystal plane ($2\theta = 50.76°$) is obviously enhanced, which indicates that the preferred orientation of the coating crystal grains appears. As shown in Fig. 3e, f, the growth direction of columnar crystals is more perpendicular to the direction of the fusion line, that is, the solidification direction of the molten pool. When WC content increases to 20 wt%, a few new diffraction peaks of M_6C appear, and the content of the γ-(Ni, Fe) phase is significantly reduced. Diffraction peaks of the same type of carbides are often overlapped, so it is difficult to accurately determine the specific composition of carbides by XRD. Moreover, a single WC phase is still not found in Fig. 4, indicating that WC has completely melted during the laser cladding process and reacted with the molten pool metal. According to the study by Fesharaki et al. [28], after laser cladding of Inconel 625 powder on Inconel 738 substrate, the phases of the cladding layer were γ-(Ni) + NbC + Laves. In comparison, it is found that, because of the addition of cobalt-coated WC in this experiment, some $M_{23}C_6$ and M_6C phases appear, and the formation of the Laves phase is suppressed.

SEM images of the middle part of the composite coatings with different WC contents are shown in Fig. 5. When WC content is 10 wt% or 15 wt%, the middle part of the coating is mainly dendritic (DR) and interdendritic (ID) with a typical lamellar eutectic morphology. However, when WC content is 20 wt%, two different microstructures appear in the middle of the coating. Figure 5d–f shows the microstructures of the coating from the top to the area near the red dash boundary line in Fig. 5c (i.e., Layers 2 and 3), in which the top of the coating is mostly developed columnar dendrites, the directionality of dendrite growth is weak, and intersects occur (Fig. 5d). Then, columnar crystals and cellular crystal regions appear, a large amount of white precipitates begin to precipitate from the grain boundaries (Fig. 5e), and cross-distributed dendrites appear below the boundary line (i.e., Layer 2) (Fig. 5f). As the cladding layer solidifies from the substrate to the surface, the dendrites after crystallization will release the latent heat of crystallization downward, so that the dendrites below have a negative temperature gradient perpendicular to the primary crystal axis [20]. The secondary crystal axis can continue to grow, and even the tertiary crystal axis may appear, which obviously refines the solidification structure of the coating.

Table 2 lists the chemical compositions of different regions of the coatings corresponding to Fig. 5. Elements such as C, Nb and Mo are mainly concentrated in grain boundaries or in interdendritic regions of columnar and cellular crystals (ID regions in Fig. 5a, b, e) and in dendrites (DR regions in Fig. 5d, f). Combined with XRD results in Fig. 4, this indicates that a large amount of carbides exist in these regions, and more γ-(Ni, Fe) solid

Fig. 5 SEM images of laser cladding coatings with WC contents of **a** 10 wt%, **b** 15 wt% and **c–f** 20 wt%

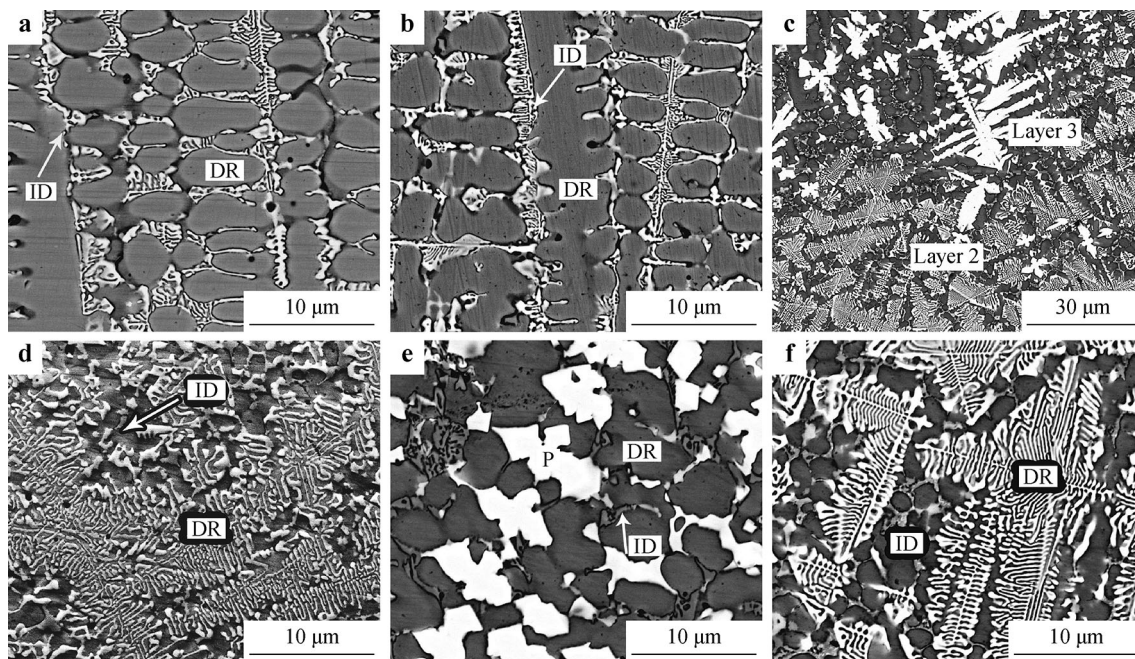**Table 2** EDS analysis results of composite coatings at different regions in Fig. 5 (wt%)

WC content/wt%	Regions	C	Si	Nb	Mo	Cr	Fe	Co	Ni	W
10	DR (Fig. 5a)	0.59	0.80	0.79	4.30	17.09	5.98	1.89	62.58	5.98
	ID (Fig. 5a)	2.34	2.37	4.39	13.58	21.52	3.70	1.45	41.91	8.75
15	DR (Fig. 5b)	0.81	0.80	0.67	3.81	16.84	13.86	1.91	56.21	5.10
	ID (Fig. 5b)	1.95	0.81	1.67	7.27	21.57	11.42	2.08	45.33	7.89
20	DR (Fig. 5d)	2.22	1.43	2.57	6.93	15.97	5.81	2.18	50.19	12.69
	ID (Fig. 5d)	0.90	1.07	1.38	3.76	16.46	7.10	2.71	58.27	8.35
	DR (Fig. 5e)	0.65	0.61	0.28	1.31	12.66	17.81	4.19	55.24	7.25
	ID (Fig. 5e)	3.42	0.38	1.31	3.60	27.24	15.94	3.19	42.49	2.43
	P (Fig. 5e)	2.28	1.54	2.68	8.57	12.70	6.22	1.36	23.42	41.22
	DR (Fig. 5f)	2.10	1.39	1.85	5.00	12.87	15.22	3.10	33.41	25.05
	ID (Fig. 5f)	0.52	0.50	0.23	1.39	13.80	24.66	4.30	48.56	6.05

solutions exist in the columnar crystal and the intracellular or interdendritic crystal. In contrast, the white bulk material deposited along the grain boundary in Fig. 5e contains a large amount of W (41.22 wt%), and the contents of Nb and Mo also increase with respect to that in the intragranular and grain boundaries.

To further confirm the phase variation in different morphologies in WC coatings, EPMA elemental mapping analysis was conducted for the 20 wt% WC coating because it exhibits more phases and has a more complex microstructure. The analysis area was selected near the interface of Layers 2 and 3 in the 20 wt% WC coating to identify the specific components of carbides, as shown in

Fig. 6. It is obvious that the phase having a morphology of white strips or blocks with directional solidification characteristics is enriched in W and Mo, which can be identified as M_6C (more precisely $(W, Mo)_6C$) according to XRD and EDS results. Nb is uniformly dispersed along grain boundaries, as shown by the white irregular granular precipitates or eutectic structure in Fig. 6a, which can be considered in the form of NbC. Cr is almost always enriched at the grain boundaries and exists in the form of $Cr_{23}C_6$, which is consistent with the higher Cr content of ID (Fig. 5e) in Table 2 and XRD results in Fig. 4. In addition, the distributions of Ni, Fe and Co in the matrix are very similar and these elements are in the form of a
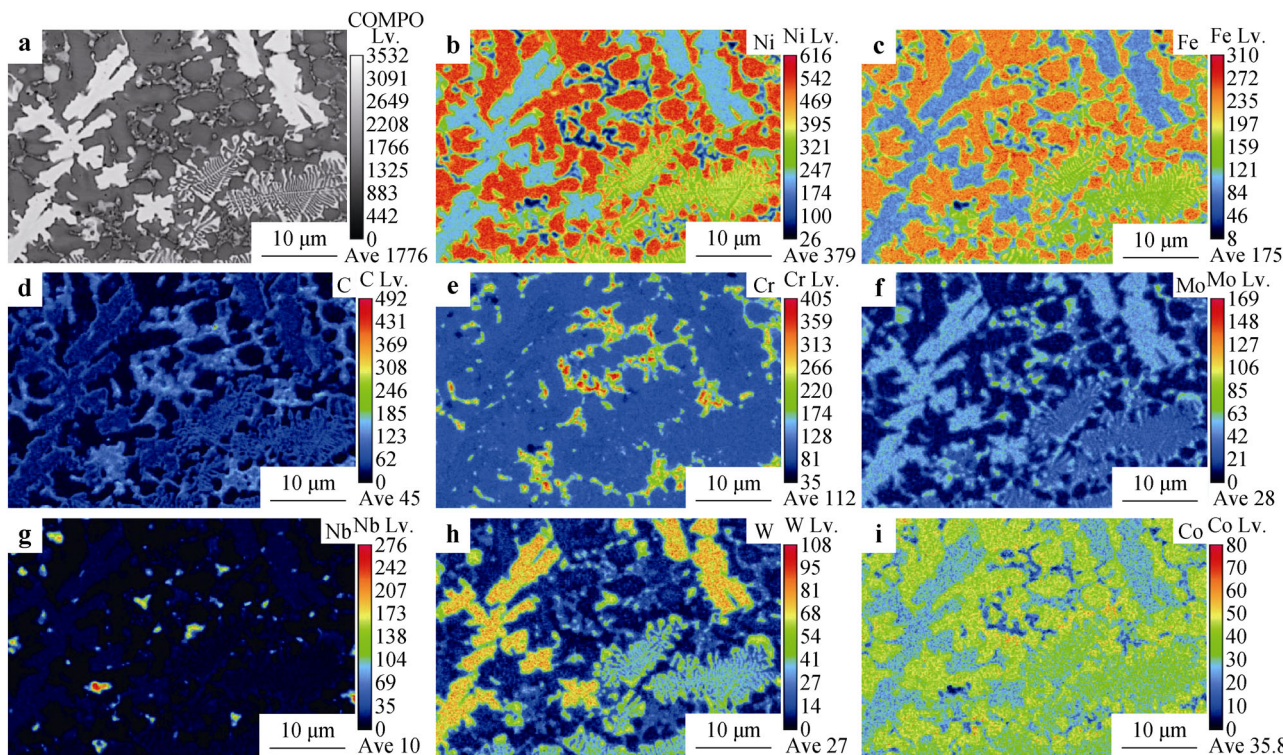
Fig. 6 **a** SEM image and EPMA elemental mapping analysis (**b** Ni, **c** Fe, **d** C, **e** Cr, **f** Mo, **g** Nb, **h** W and **i** Co) results of 20 wt% WC coating (Lv., level; COMPO, composition; Ave, average)
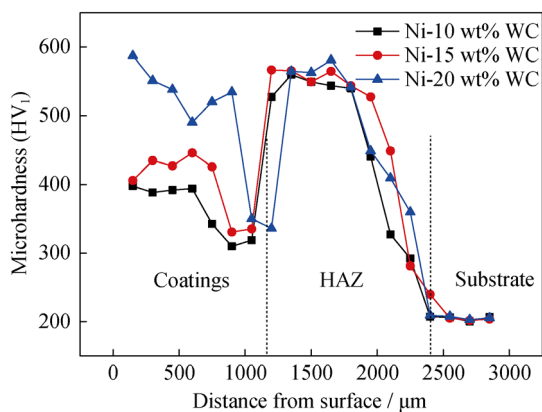

Fig. 7 Microhardness distribution of laser cladding layers with different WC contents

solid solution state in the Ni matrix, which indicates that the Co introduced from the Co-coated tungsten carbide does not form a new phase during the cladding process.

3.3 Microhardness

Figure 7 shows the microhardness distribution curves of composite coatings along the depth direction. It can be seen that the portion of the bottom bonding region of the coating (planar crystal and columnar crystal region) has a relatively lower hardness compared to the surface layer and the middle portion because of the dilution of the substrate. In addition, the heat-affected zone (HAZ) is greatly affected by the laser heat input during the cladding process. Martensite transformation occurs during rapid cooling, and a quenched martensite structure is formed. Therefore, the hardness of the HAZ is much higher than that of the substrate. As WC content in the coating increases, the average hardness of the coating also increases. The average hardness values for the composite coatings with 10 wt%, 15 wt% and 20 wt% WC are HV_1 382.84, HV_1 427.82 and HV_1 536.98, respectively, which correspond to factors of 1.89, 2.12 and 2.64 times higher than the hardness of the 2Cr13 steel substrate (HV_1 202). Normally, the hardness and strength of metallic materials are generally positively correlated. According to the Hall–Petch equation [29, 30], as the grain refines (i.e., d decreases), the yield strength (σ_s) of the material will increase. Thus, the increase in hardness of the 15 wt% WC coating compared to that of the 10 wt% WC coating can be partly attributed to the refinement of the microstructure of the cladding layer. When WC content is 20 wt%, Layers 2 and 3 consist mostly of dendritic eutectic structures (γ-(Ni, Fe) + carbides), while numerous white bulk carbides are precipitated at the cellular grain boundaries of Layer 3. The microhardness of the 20 wt% WC coating is greatly improved by the combined effect of fine grain strengthening and precipitation strengthening.
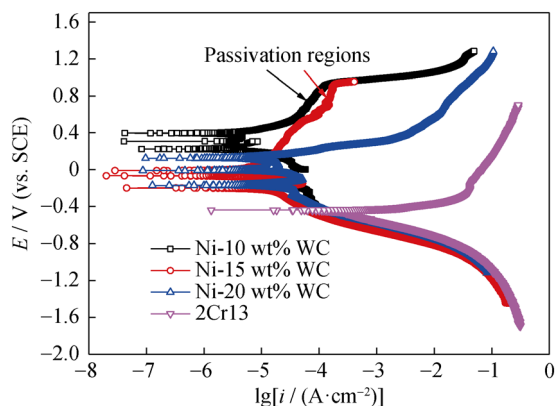
Fig. 8 Dynamic potential polarization curves of composite coatings and 2Cr13 steel in 0.5 mol·L^{-1} HCl solution

3.4 Electrochemical performance

Figure 8 shows electrochemical performance of the composite coatings and 2Cr13 steel in 0.5 mol·L^{-1} HCl solution. In the anodic dissolution zone of 2Cr13 steel (potential interval of − 0.43 to − 0.25 V), the potential density increases obviously with the increase in potential, which is characterized by active dissolution. This is due to the rapid dissolution of Fe, Cr and other elements, resulting in the formation of cations, and the dissolution rate of the anode is much higher than the formation rate of the passive film on its surface. When the applied voltage is increased, a very short passivation zone appears on the surface of 2Cr13 steel in the potential range of − 0.25 to − 0.11 V. Active metal ions such as Fe and Cr ions are combined with O^{2-} in the HCl solution as a result of adsorption [31]. A thin passivation film layer forms on the surface of 2Cr13 steel, and this layer consists of oxides such as Fe_3O_4 and Cr_2O_3. However, with the increase in applied voltage, the dissolution rate of the passive film on the surface of the sample is much higher than the formation rate, which enhances the anodic activity of the dissolution process on the surface of the sample significantly and causes the passive film to lose its protective effect very quickly. The serious corrosion on the sample surface is strongly consistent with the results for other stainless steels in a strong acid medium [32]. For these three kinds of composite coatings, their polarization degrees are all above that of 2Cr13 steel, indicating that they have a positive self-corrosion potential. In the anodic polarization region, there are three plateau potentials, but the potential and interval of each plateau are different. For the first plateau, the potential decreases rapidly after the plateau appearing, which is the transition from activation to passivation of the electrode reaction. However, the potential interval of the passivation region is very small, indicating that the passivation film is dissolved quickly after its formation. The appearance of the second plateau potential

reveals that a new reaction may have occurred here. A new passivation film is produced, but it is dissolved immediately after its appearance. After the third plateau, the corrosion process enters a typical anode activation zone and a pitting potential begins to appear. Among these three coatings, the largest passivation potential of 0.55–0.93 V occurs for the composite coating with WC content of 10 wt%, and its value drops to 0.70–0.94 V for the 15 wt% WC coating.

The Ni-based powder contains large quantities of alloy elements such as Cr (20.21 wt%), Mo (9.22 wt%) and the matrix element Ni (> 60 wt%). According to the adsorption theory of passivation film formation [32, 33], the combination of active metal ions with O^{2-} from the HCl solution on the surface of the sample increases the corrosion potential of the metal and suppresses the corrosion dissolution reaction of the metal and the solution. With an increase in the applied voltage, passivation films with high thermodynamic stabilities (such as Fe_3O_4, NiO and Cr_2O_3) begin to form gradually. In general, the formation rate of the passivation film is greater than dissolution rate, so the corrosion current density increases slowly in the passivation interval, manifesting the protective effect of the passivation film. The chemical properties of Ni are stable, which can reduce the anodic dissolution rate and improve the corrosion resistance and passivation ability of the coating [32, 34, 35]. However, when WC content reaches 20 wt%, no passivation zone appears. In addition, it can be seen that the anodic polarization curves of the 15 wt% and 20 wt% composite coatings were all located below that of the 10 wt% WC coating. The reduced corrosion resistance of the coating can be attributed to the relatively lower Ni content in the coating caused by the higher WC content.

Tafel fitting was performed on the parameters of the polarization curve to obtain the self-corrosion potential (E_{corr}), the self-corrosion current density (i_{corr}) and the polarization resistance (R_p). The fitting results are given in Table 3. It can be seen from Fig. 8 and Table 3 that the cathode polarization curves of the three composite coatings and the substrate are substantially the same. Compared with 2Cr13 steel, E_{corr} values of the 10 wt%, 15 wt% and 20 wt% composite coatings are 0.30864, − 0.12603 and − 0.02047 V, respectively, and all of them exhibit a

Table 3 Fitting results of potential dynamic polarization curves in 0.5 mol·L^{-1} HCl solution

Materials	E_{corr}/V	i_{corr}/(A·cm^{-2})	R_p/Ω
Ni–10 wt% WC coating	0.30864	2.7430×10^{-6}	4089.100
Ni–15 wt% WC coating	−0.12603	7.4685×10^{-6}	1327.400
Ni–20 wt% WC coating	−0.02047	1.9648×10^{-5}	1328.400
2Cr13	−0.47942	3.1813×10^{-4}	21.928

positive shift, indicating that the corrosion resistances of all the composite coatings are better than that of the 2Cr13 steel matrix. At the same time, the i_{corr} values of the three composite coatings are significantly reduced compared to that of 2Cr13 steel. i_{corr} value of the 10 wt% WC coating (2.7430×10^{-6} A·cm^{-2}) is only 0.86% that of 2Cr13 steel (3.1813×10^{-4} A·cm^{-2}), and the polarization resistance (R_p) is 186 times higher than that of 2Cr13 steel. Based on the comprehensive analysis above, it can be concluded that the 10 wt% WC composite coating has the best corrosion resistance.

Figure 9 shows EIS spectra of the composite coatings and 2Cr13 steel in 0.5 mol·L^{-1} HCl solution. It can be seen from the Nyquist plots (Fig. 9a) that the impedance spectrum of 2Cr13 steel in a 0.5 mol·L^{-1} HCl solution consists of a high-frequency capacitive reactance loop and a low-frequency inductive loop, which is a typical impedance spectrum of alloy steel in strongly acidic corrosive media [36]. The high-frequency capacitive reactance loop is closely related to the electron transfer process on the surface of the sample, while the low-frequency inductive loop is mainly caused by the adsorption of corrosion products on the surface of the sample. However, the three composite coatings exhibit a capacitive reactance loop throughout the impedance spectrum, indicating that the electrode reaction is an interfacial reaction control process over the test frequency range. The larger the radius of the loop is, the larger the total impedance of the sample is, and the better the corrosion resistance is [37, 38]. The 10 wt% WC composite coating has a much larger capacitive reactance loop than the other two composite coatings, indicating that 10 wt% WC composite coating has the best corrosion resistance. The impedance (|Z|) of the low-frequency region (0.01–1.00 Hz) reflects the impedance of the corrosion reaction [39, 40]. It can be seen from the Bode curves (Fig. 9b) that the impedance of the three composite coatings in this frequency range is much higher than that of 2Cr13 steel. This demonstrates that the aggressive ions in the HCl solution have greater difficulty in acting on the

substrate through the passivation film on the surface of the composite coating, so the composite coating acts as an effective protection barrier to the substrate in 0.5 mol·L^{-1} HCl solution. Generally, the ability of the composite coating to inhibit electrode penetration is related to the peak of the phase angle of the intermediate frequency region [39]. The higher the peak value is, the better the corrosion resistance is. It can be seen from Fig. 9c (Bode curves) that the phase angles (θ) of the three composite coatings reach maxima in the range of 10–1000 Hz. The 10 wt% WC composite coating has the highest θ_{max} (close to $-90°$), which indicates that the passivation film on the surface of the sample tends to be a pure capacitor insulation layer, and the passivation film has strong protection ability for the sample. According to the polarization curves (Fig. 8) and EIS curves (Fig. 9), the corrosion resistances of these three composite coatings are better than that of 2Cr13 steel. The highest corrosion resistance is achieved by the composite coating with 10 wt% WC, and the corrosion resistance of the composite coating with 20 wt% WC is slightly greater than that of 15 wt% WC coating.

4 Conclusion

Inconel 625 + WC composite coatings without oxide inclusions, cracks or other defects can be prepared on the surface of 2Cr13 steel substrate under suitable laser cladding process parameters, and they exhibit good metallurgical bonding with the substrate. WC content has little effect on the phase composition of the composite coatings, but it significantly affects the microstructure. The microstructures of composite coatings with WC contents of 10 wt% and 15 wt% are similar and are mainly composed of columnar dendrites. When WC content is 20 wt%, the structures in middle and top of the coating are mostly dendrites, and numerous blocky carbides are precipitated. Moreover, the original WC particles cannot be observed in all the three coatings. When WC content is 10 wt%, the
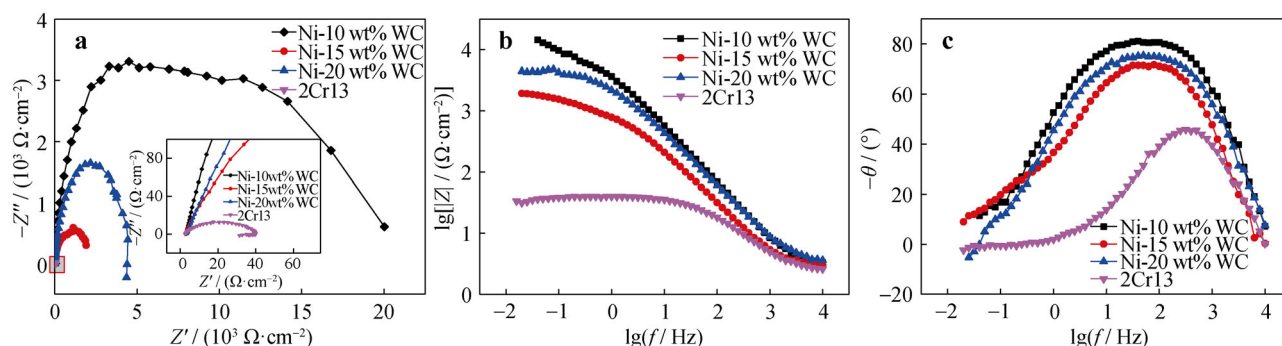

Fig. 9 EIS spectra of different samples in 0.5 mol·L^{-1} HCl solution: **a** Nyquist plots and **b**, **c** Bode plots (Z', real part of impedance; Z'', imaginary part of impedance)

composite coating has the best corrosion resistance. And when WC content is 20 wt%, the average hardness of the composite coating is the highest.

References

[1] Wen ZH, Bai Y, Yang JF, Huang J. Effect of vacuum re-melting on the solid particles erosion behavior of Ni60–NiCrMoY composite coatings prepared by plasma spraying. Vacuum. 2016;134:73.

[2] Mann BS, Arya V. HVOF coating and surface treatment for enhancing droplet erosion resistance of steam turbine blades. Wear. 2003;254(7):652.

[3] Dong XC. A study on the corrosion and wearing of TRT blades. Metal Power. 2015;179(1):40.

[4] Shitarev IL, Smelov VG, Sotov AV. Repair of a gas turbine blade tip by impulse laser build-up welding. Appl Mech Mater. 2014;682:96.

[5] Tian JJ, Yao SW, Luo XT, Li CX, Li CJ. An effective approach for creating metallurgical self-bonding in plasma-spraying of NiCr–Mo coating by designing shell–core-structured powders. Acta Mater. 2016;110:19.

[6] Jafari M, Enayati MH, Salehi M, Nahvr SM, Park CG. Microstructural and mechanical characterizations of a novel HVOF-sprayed WC–Co coating deposited from electroless Ni–P coated WC–12Co powders. Mater Sci Eng A. 2013;578:46.

[7] Shepeleva L, Medres B, Kaplan WD, Bamberger M, Weisheit A. Laser cladding of turbine blades. Surf Coat Technol. 2000;125(1):45.

[8] Calleja A, Tabernero I, Ealo JA, Campa FJ, Lamikiz A, Lacalle LN. Feed rate calculation algorithm for the homogeneous material deposition of blisk blades by 5-axis laser cladding. Int J Adv Manuf Technol. 2014;74(9–12):1219.

[9] Brandt M, Sun S, Alam N, Bendeich P, Bishop A. Laser cladding repair of turbine blades in power plants: from research to commercialisation. Int Heat Treat Surf Eng. 2013;3(3):105.

[10] Özgün O, Gülsoy HO, Yilmaz R, Findik F. Microstructural and mechanical characterization of injection molded 718 superalloy powders. J Alloys Compd. 2013;576:140.

[11] Özgün O, Gülsoy HO, Findik F, Yilmaz R. Microstructure and mechanical properties of injection moulded Nimonic-90 superalloy parts. Powder Metall. 2012;55(5):413.

[12] Quadbeck P, Kaschta J, Singer RF. Superalloy IN625 with cellular microstructure-fabrication route and mechanical properties. Adv Eng Mater. 2004;6(8):635.

[13] Bao HS, Gong ZH, Chen ZZ, Yang G. Evolution of precipitates in Ni–Co–Cr–W–Mo superalloys with different tungsten contents. Rare Met. 2020;39(6):716.

[14] Özgün O, Yilmaz R, Gülsoy HO, Findik F. The effect of aging treatment on the fracture toughness and impact strength of injection molded Ni-625 superalloy parts. Mater Charact. 2015;108:8.

[15] Niaz A, Khan S. A comprehensive pitting study of high velocity oxygen fuel Inconel 625 coating by using electrochemical testing techniques. J Mater Eng Perform. 2015;25(1):1.

[16] Xu FJ, Lv YH, Liu YX, Shu FY, He P, Xu BS. Microstructural evolution and mechanical properties of Inconel 625 alloy during pulsed plasma loop deposition process. J Mater Sci Technol. 2013;29(5):480.

[17] Ahmed N, Voisey KT, Mccartney DG. Supplementary microstructural features induced during laser surface melting of thermally sprayed Inconel 625 coatings. J Them Spray Technol. 2014;23(3):402.

[18] Nurminen J, Näkki J, Vuoristo P. Microstructure and properties of hard and wear resistant MMC coatings deposited by laser cladding. Int J Refract Met Hard. 2009;27(2):472.

[19] Przybyłowicz J, Kusiński J. Structure of laser cladded tungsten carbide composite coatings. J Mater Process Technol. 2001;109(1–2):154.

[20] Weng Z, Wang A, Wu X, Wang YY, Yang ZX. Wear resistance of diode laser-clad Ni/WC composite coatings at different temperatures. Surf Coat Technol. 2016;304:283.

[21] Wang KM, Lei YP, Wei SZ, Fu HG, Yang YW, Li YL, Su ZQ. Effect of WC content on microstructure and properties of laser cladding Ni-based WC composite coating. Trans Mater Heat Treat. 2016;37(7):172.

[22] Zhou SF, Huang YJ, Zeng XY. Effects of processing parameters on structure of Ni-based WC composite coatings during laser induction hybrid rapid cladding. Appl Surf Sci. 2009;255(20):8494.

[23] Yuan YL, Li ZG. Dissolving and precipitating characteristics of WC and carbides in the Ni60A + WC graded coating. J Mater Eng. 2013;11:12.

[24] Shao JZ, Li J, Song R, Bai LL, Chen JL, Qu CC. Microstructure and wear behaviors of TiB/TiC reinforced Ti₂Ni/α(Ti) matrix coating produced by laser cladding. Rare Met. 2020;39(3):304.

[25] Zhou SF, Huang YJ, Zeng XY, Hu QW. Microstructure characteristics of Ni-based WC composite coatings by laser induction hybrid rapid cladding. Mater Sci Eng A. 2008;480(1–2):564.

[26] Zhong ML, Liu WJ, Yao KF, Goussain JC, Mayer C, Becker A. Microstructural evolution in high power laser cladding of Stellite 6 + WC layers. Surf Coat Technol. 2002;157(2–3):128.

[27] Rong L, Huang J, Li ZG, Li RF. Microstructure and property of laser cladding Ni − based alloy coating reinforced by WC particles. Chin Surf Eng. 2010;23(6):40.

[28] Fesharaki MN, Reza SR, Mansouri HA, Jamali H. Microstructure investigation of Inconel 625 coating obtained by laser cladding and TIG cladding methods. Surf Coat Technol. 2018;353:25.

[29] Suarez S, Lasserre F, Mücklich F. Mechanical properties of MWNT/Ni bulk composites: influence of the microstructural refinement on the hardness. Mater Sci Eng A. 2013;587:381.

[30] Liu L, Li WW, Tang YP, Shen B, Hu WB. Friction and wear properties of short carbon fiber reinforced aluminum matrix composites. Wear. 2009;266(7):733.

[31] Jiang CP. The Microstructure and Properties of Fe-Based Amorphous Coatings Fabricated by Plasma Spraying. Xi'an: Chang'an University; 2015. 82.

[32] Hu YB, Dong CF, Sun M, Xiao K, Zhong P, Li XG. Effects of solution pH and Cl⁻ on electrochemical behaviour of an Aermet100 ultra-high strength steel in acidic environments. Corros Sci. 2011;53(12):4159.

[33] Andreev YY. Adsorption equilibrium at the metal-oxide film interface in the oxidation reactions of Ni, Cr, and their alloys. Russ J Phys Chem A. 2007;81(6):967.

[34] Lei JB, Shi C, Zhou SF, Gu ZJ, Zhang LC. Enhanced corrosion and wear resistance properties of carbon fiber reinforced Ni-based composite coating by laser cladding. Surf Coat Technol. 2018;334:274.

[35] Li F, Chen HY, Dong YH, Li XY, Dong LH, Yin YS. Corrosion behavior of Fe-based laser cladding coating in hydrochloric acid solutions. Acta Metal Sin. 2018;54(7):1019.

[36] Atta AM, Allohedan HA, El-Mahdy GA, Ezzat ARO. Application of stabilized silver nanoparticles as thin films as corrosion

inhibitors for carbon steel alloy in 1 M hydrochloric acid. J Nanomater. 2013;48:132.

[37] Wu LF, Li T, Zhao HY, Sun MS, Fan J. Influence of Ce on corrosion resistance of 2A12 aluminum alloy in harsh marine atmospheric. Chin J Rare Met. 2019;43(12):1269.

[38] Cao CN. Principles of Electrochemistry of Corrosion. Beijing: Chemical Industry Press; 2008. 176.

[39] Dai NW, Zhang LC, Zhang JX, Zhang X, Ni QZ, Chen Y, Wu ML, Yang C. Distinction in corrosion resistance of selective laser melted Ti–6Al–4 V alloy on different planes. Corros Sci. 2016;111:703.

[40] Wen ZH, Bai Y, Yang JF, Huang J. Corrosion resistance of vacuum re-melted Ni60–NiCrMoY alloy coatings. J Alloys Compd. 2017;711:659.